Radiation Fluxes in a Business District of Shanghai, China

XIANGYU AO,[a] C. S. B. GRIMMOND,[b] DONGWEI LIU,[a] ZHIHUI HAN,[a] PING HU,[c]
YADONG WANG,[c] XINRONG ZHEN,[d] AND JIANGUO TAN[a,d]

[a] *Shanghai Institute of Meteorological Science, Shanghai Meteorological Service, Shanghai, China*
[b] *Department of Meteorology, University of Reading, Reading, United Kingdom*
[c] *Shanghai Meteorological Information and Technological Support Centre, Shanghai, China*
[d] *Shanghai Key Laboratory of Meteorology and Health, Shanghai Meteorological Service, Shanghai, China*

ABSTRACT

Radiative fluxes are key drivers of surface–atmosphere heat exchanges in cities. Here the first yearlong (December 2012–November 2013) measurements of the full radiation balance for a dense urban site in Shanghai, China, are presented, collected with a CNR4 net radiometer mounted 80 m above ground. Clear-sky incoming shortwave radiation $K_\downarrow$ (median daytime maxima) ranges from $575\,\mathrm{W\,m^{-2}}$ in winter to $875\,\mathrm{W\,m^{-2}}$ in spring, with cloud cover reducing the daily maxima by about $160\,\mathrm{W\,m^{-2}}$. The median incoming longwave radiation daytime maxima are 305 and $468\,\mathrm{W\,m^{-2}}$ in winter and summer, respectively, with increases of 30 and $15\,\mathrm{W\,m^{-2}}$ for cloudy conditions. The effect of air quality is evident: haze conditions decrease hourly median $K_\downarrow$ by 11.3%. The midday (1100–1300 LST) clear-sky surface albedo α is 0.128, 0.141, 0.143, and 0.129 for winter, spring, summer, and autumn, respectively. The value of α varies with solar elevation and azimuth angle because of the heterogeneity of the urban surface. In winter, shadows play an important role in decreasing α in the late afternoon. For the site, the bulk α is 0.14. The Net All-Wave Radiation Parameterization Scheme/Surface Urban Energy and Water Balance Scheme (NARP/SUEWS) land surface model reproduces the radiation components at this site well, which is a promising result for applications elsewhere. These observations help to fill the gap of long-term radiation measurements in East Asian and low-latitude cities, quantifying the effects of season, cloud cover, and air quality.

1. Introduction

Radiative fluxes (shortwave and longwave) are the key drivers of surface exchanges of heat. However, for most cities worldwide, long-term measurements of these fluxes are lacking. Here the first yearlong measurements of the full radiation balance for a dense urban site in Shanghai (China) are presented, along with an evaluation of a simple model for their prediction. Of particular interest are differences with season and cloud cover, as well as the effects of air quality.

Radiative exchanges are impacted by the material characteristics of the urban surface (Aida and Gotoh 1982), urban form (Aida 1982), and urban atmosphere (Qian et al. 2006). The surface albedo ($\alpha = K_\uparrow / K_\downarrow$, which is the ratio of the reflected to the incoming solar shortwave radiation flux) has received particular attention, given that it is a critical parameter in the performance of numerical land surface models (e.g., Masson 2000; Offerle et al. 2003; Loridan et al. 2010; Zhao et al. 2014) and its modification provides potential for altering local-scale urban climate. For example, it has been proposed that changing roof materials (higher albedo) could mitigate the urban heat island effect in summer (Akbari et al. 1997, 2012, Bretz and Akbari 1997; Mackey et al. 2012; Li et al. 2014; Raman et al. 2014).

The framework used in this paper is the surface radiation budget, which combines the incoming ($\downarrow$) and outgoing ($\uparrow$) shortwave (K) and longwave (L) radiation fluxes to give the net all-wave radiation available for convection and conduction:

$$Q* = (K_\downarrow - K_\uparrow) + (L_\downarrow - L_\uparrow). \qquad (1)$$

Components of the atmosphere absorb, reflect, and scatter the incoming solar radiation resulting in a reduction of the shortwave radiation reaching the surface.

Corresponding author address: Jianguo Tan, Shanghai Meteorological Service, Shanghai Institute of Meteorological Science, 166 Puxi Road, Shanghai, 200030, China.
E-mail: tanjg@mail.typhoon.gov.cn

Solar radiation is absorbed by gases (O_2, O_3, H_2O, CO_2, CH_4, and N_2O; Oke 1987) but also is affected by high concentrations of atmospheric aerosols causing solar dimming (reduced atmospheric transmissivity and visibility), which significantly influences the receipt of solar radiation at the surface (Qian et al. 2006; Wang et al. 2012b; Wild 2012; Ding et al. 2013; Jiang et al. 2013; Nie et al. 2014). Incoming longwave radiation flux ($L_\downarrow$) also is influenced by cloud cover, cloud type, greenhouse gases, and aerosols (Wang and Dickinson 2013). In land surface models it is more difficult to estimate $L_\downarrow$ than $K_\uparrow$ because of the complex variability of cloud (cloud fraction, type, and height) and atmospheric aerosols (Offerle et al. 2003). Tall buildings in cities trap radiation, thereby reducing both the effective albedo and the outgoing longwave radiation. This is a primary cause of the urban heat island effect (Oke 1982; Kondo et al. 2001).

Although direct measurements of the four components of the net all-wave radiation [Eq. (1)] in urban areas are needed for a wide range of applications, there are still remarkably few long-term measurements. Observations in cities are challenging because of complex urban surface–sensor–sun relations (Soux et al. 2004), the wide range of surface materials (Kotthaus et al. 2014) and their arrangements (e.g., Kotthaus and Grimmond 2014a,b), and logistical factors involved in siting equipment (Offerle et al. 2003). In densely built up cities with many tall buildings, the radiometer sensor height needs to be approximately 2.5 times that of the mean building height to measure representative local-scale radiation fluxes (Offerle et al. 2003; Roberts 2010).

Despite these complexities and challenges, a relatively small number of urban field studies of surface radiation exist. However, these have done much to enhance the understanding of the processes of the urban radiation budget (e.g., Grimmond et al. 1996; Christen and Vogt 2004; Moriwaki and Kanda 2004; Miao et al. 2012; Ward et al. 2013). Most urban measurements have been conducted over relatively low-rise buildings (suburban sites) with little analysis of temporal variations of the radiation fluxes and their controls [exceptions include Schmid et al. (1991) and Kotthaus and Grimmond (2014a,b)]. Some studies include observations of radiation to help explain other processes. For example, the primary focus of Moriwaki and Kanda's (2004) was the turbulent heat flux partitioning (sensible and latent heat flux) in a residential area of Tokyo (mean building height: 7.3 m), with net radiation fluxes mentioned only as a driver of these processes. The mean diurnal patterns of the four components of radiation are reported only for two months (July and December).

In East Asia, ground-based radiation observations remain minimal. In China, for example, the focus has been on natural surfaces, such as the Tibetan Plateau and Gobi Desert (Wang et al. 2005; Wang et al. 2008; Li et al. 2010; Zhang et al. 2013). In Beijing, Miao et al. (2012) report measurements from the 325-m tower, but these have not yet been published in detail. To our knowledge, the radiation measurements presented here are the only full year study conducted in a central business district in China.

The objective of this study is to investigate temporal (diurnal and seasonal) variations of surface radiation fluxes in Shanghai based on 1 yr of measurements in a neighborhood with tall buildings. Particular attention is directed to the impact of the complex three-dimensional urban canyon structure, solar geometry, and air quality on the solar radiation and surface albedo. The measurements are used to evaluate the radiation scheme in the land surface model Surface Urban Energy and Water Balance Scheme (SUEWS). This research can inform the understanding of the energetic basis of urban atmospheric processes, such as the urban heat island (UHI; e.g., albedo or net all-wave radiation differences) for which there is extensive interest (e.g., Li et al. 2009; Wang et al. 2015; Li et al. 2015; Zhou et al. 2015; Sun et al. 2016).The data presented also have important utility for an array of applications, especially evaluations of land surface models, that can be used to contribute to the comfort, health, and safety of city inhabitants and be instructive to urban planners and decision-makers.

2. Methods

a. The site

Shanghai, the economic, financial, shipping, and trade capital of China, has grown rapidly since 1970. Numerous tall buildings have been built to accommodate a population density of more than 15 000 people per square kilometer (Shi and Cui 2012). Similar to large parts of central Shanghai, the study site is a densely built commercial and residential area, with pockets of educational and scientific institutions. The measurement site, located in Xujiahui (XJH; 31.19°N, 121.43°E), at the headquarters of the Shanghai Meteorological Service, has a long history of meteorological observations (Tan et al. 2015).

b. Observations

A net radiometer (model CNR4 from Kipp & Zonen B.V.) mounted 80 m above ground level (AGL) (atop a 25-m tower installed on a 55-m-high building) is connected to a CR3000 datalogger (Campbell Scientific, Inc.). The CNR4's four independent sensors (two pyranometers and two pyrgeometers) measure the four

components of net all-wave radiation independently. The spectral response of the instrument is between 0.3 and 2.8 μm for shortwave radiation and between 4.5 and 42 μm for the far infrared or longwave radiation (Kipp & Zonen 2014). This model has been found to be more accurate than net radiometers (e.g., Kipp & Zonen NR lite) that do not measure the individual components (Blonquist et al. 2009; Wang et al. 2012a). Prior to installation, the CNR4 sensor was calibrated by the manufacturer. The instrument is sampled every 1 min, and 30-min averages are recorded. The instrument has a response time (95%) of <18 s. Quality-control processing includes forcing nocturnal shortwave radiation to 0 W m^{-2} (Michel et al. 2008). For the yearlong study period, after quality control, 86.0% ($N = 15\,071$) of the 30-min periods are available. Losses of data are due to power failure, instrument malfunction, or maintenance for short periods (e.g., 11–17 December 2012 and 8–16 March 2013; Table 1). During rain events, water deposition on the sensor window or domes will obstruct the far infrared radiation and may increase measurement errors. However, these errors are likely small as the signal will be close to zero (Kipp & Zonen 2014).

The data analyzed are for the year from 1 December 2012 to 30 November 2013. All data referred to are local time and time ending; 1100 refers to data collected from 1030:01 to 1100. Daylight savings time is not used in Shanghai. The four seasons of a year are defined based on the commonly used classification in China: winter [December–February (DJF)], spring [March–May (MAM)], summer [June–August (JJA)], and autumn [September–November (SON)].

Manually observed cloud cover and cloud type were taken at the XJH observatory three times per day (0800, 1400, and 2000 LST) until October 2013. Based on observed daytime cloud-cover data (0800 and 1400 LST) and hourly rainfall data, the daily sky conditions are classified into clear, cloudy, overcast, and rainy (Table 1). That is, when the cloud cover at both 0800 and 1400 LST is less than 20%, or the diurnal curve of $K_\downarrow$ is very smooth, the day is defined as a clear day; if the daytime cloud cover is between 30% and 80%, it is a cloudy day; if the daytime cloud cover is more than 80%, it is an overcast day; if it rained at all during a day, it is a rainy day. The occurrence of weather phenomena, such as the time of rain, snow, fog, dew, and haze, was also recorded. Precipitation data are obtained from the automated meteorological station (AWS; Vaisala, Inc., MILOS500) located 60 m from the tower site. Particulate matter (PM) of 2.5 μm or smaller size is measured at around 50 m AGL (atop a building, about 50 m to the south from the CNR4 sensor) using a Thermo Fisher Scientific, Inc., 5030 SHARP Monitor. The 1-min samples

are averaged to provide hourly means. Following Xiao et al. (2011) and Zhang and Cao (2015), clear or cloudy days are subdivided into haze or no-haze hours based on observed hourly visibility (Vaisala PWD22), relative humidity (RH), and PM$_{2.5}$ concentration; that is, if the hourly visibility on clear or cloudy days is longer than 10 km and PM$_{2.5}$ is less than 35 μg m^{-3}, the hours are defined as clear (or cloudy, as appropriate) no haze; whereas if the hourly visibility for clear or cloudy days is less than 10 km, relative humidity is less than 90%, and PM$_{2.5}$ is larger than 35 μg m^{-3}, the hours are defined as clear (or cloudy) haze. The definition and data availability for all the sky conditions are also summarized in Table 1.

Tall buildings have a complex influence on the radiation budget of an urban environment. To document the urban morphology and sky-view factors around the site, a Nikon D610 digital camera fitted with a fish-eye hemispheric lens (Sigma 8-mm f3.5) was used to take onsite photographs that produce a hemispheric projection of the radiating environment onto a circular image. The manufacturer-specified field of view (FOV) for the lens is 180° (Sigma 2013). The response time of the camera is milliseconds. Photographs were taken near the foot of the tower (i.e., at 55 m AGL). This photographic method has been used widely to estimate sky-view factors (Steyn et al. 1986; Grimmond et al. 2001; Chen et al. 2012).

c. Analysis methods

To determine the bulk atmospheric transmissivity τ, the incoming solar radiation at the surface is compared with the solar radiation flux received at the top of Earth's atmosphere ($K_{\downarrow,\text{TOA}}$):

$$\tau = K_\downarrow / K_{\downarrow,\text{TOA}}. \tag{2}$$

The larger τ is, the more transparent is the atmosphere. To calculate the incoming solar radiation at the top of the atmosphere, a solar "constant" S_0 of 1361 W m^{-2} (Kopp and Lean 2011) was used with

$$K_{\downarrow,\text{TOA}} = S_0 \left(\frac{r_0}{r}\right)^2 \sin h. \tag{3}$$

The Earth–sun distance r changes over the course of Earth's annual elliptical orbit around the sun relative to mean Earth–sun distance r_0. Here r/r_0 is calculated (Eva and Lambin 1998) as

$$r/r_0 = 1 - 0.1672 \cos[0.9856(\text{DOY} - 4)\pi/180], \tag{4}$$

where DOY is day of year. The solar elevation angle h is calculated from (Jacobson 2005)

$$\sin h = \sin\varphi \sin\delta + \cos\varphi \cos\delta \cos\omega, \tag{5}$$

where φ is the local latitude, δ is the declination of the sun, and ω is the hour angle.

3. Results and discussion

a. Characterization of the shortwave radiation

All four components of the radiation budget were observed in this study (Fig. 1). The median daytime maxima of incoming shortwave radiation for clear days ranged from $575 \, \text{W m}^{-2}$ in winter to $875 \, \text{W m}^{-2}$ in spring. As expected, this variation is much smaller than that for more northerly cities, such as London, England (52°N), where daytime maxima range from about 200 to $1000 \, \text{W m}^{-2}$ (Kotthaus and Grimmond 2014a,b), and is similar to that of the closer site of Tokyo, Japan (35.57 °N), where values range from 500 to $870 \, \text{W m}^{-2}$ (Moriwaki and Kanda 2004). These latitudinal differences are primarily due to differences in the solar elevation angle. Daily maxima of the reflected shortwave radiation ($K_\uparrow$) reported here for Shanghai, range between $80 \, \text{W m}^{-2}$ in winter and $150 \, \text{W m}^{-2}$ in summer. The extremely low values of the incoming and reflected shortwave radiation documented in June 2013 (evident in Fig. 1) are a result of persistent rainfall.

When stratified by sky conditions (Fig. 2), it is evident that cloud-cover fraction has a significant influence on the radiation fluxes. As overcast conditions without rain (Table 1) occurred on only 13 days, these are combined with cloudy conditions for the remaining analyses. Under cloudy conditions, the reduction (relative to clear conditions) of seasonal median midday (1100–1300 LST) $K_\downarrow$ is $164 \, \text{W m}^{-2}$ in winter, $128 \, \text{W m}^{-2}$ in spring, $149 \, \text{W m}^{-2}$ in summer, and $41 \, \text{W m}^{-2}$ in autumn. The largest reductions occurred in February ($370 \, \text{W m}^{-2}$) and June ($352 \, \text{W m}^{-2}$) (not shown). In June, during the East Asian rainy season (commonly called the plum rain or mei-yu), precipitation occurs along a persistent stationary mei-yu front. During the 2013 Shanghai mei-yu period (7–30 June), when the cloud fraction is largest, the clouds (Fig. 3) were always altostratus opacus (As op), stratocumulus opacus (Sc op), altocumulus opacus (Ac op), or fractonimbus (Fn). During February 2013, a continuous rainy period resulted in the second-largest mean cloud-cover fraction (Fig. 3).

On rainy days (Table 1), $K_\downarrow$ decreases markedly during winter, spring, and autumn, with seasonal median daytime peaks of only 141–$303 \, \text{W m}^{-2}$. Relative to clear conditions, the reduction of the median daytime peaks is $435 \, \text{W m}^{-2}$ in winter, $632 \, \text{W m}^{-2}$ in spring, $575 \, \text{W m}^{-2}$ in summer, and $111 \, \text{W m}^{-2}$ in autumn. The interquartile range (IQR) of the solar radiation under cloudy and mixed rainy conditions (Fig. 2), as expected, is much larger than under clear conditions.

The bulk transmissivity τ under different sky conditions is used to assess the influence of cloud, haze, and rain on $K_\downarrow$ (Figs. 4 and 5). For clear conditions, the monthly midday median (1100–1300 LST) τ is between 0.6 and 0.7, and decreases steadily from winter to spring to summer to autumn (0.69, 0.68, 0.64, and 0.63). This seasonal trend may relate to increased absorption and reflection by more water vapor in the air in the summer and autumn (Fig. 1f shows large absolute humidity values at this site in summer and autumn) and/or different seasonal composition of aerosols (Fu 2009; He et al. 2012; Zhang and Cao 2015). Although τ decreases near sunrise and sunset because of increased solar path length through the atmosphere, τ values are smaller near sunrise than sunset in most months. This may relate to the frequent presence of residual layers overnight (Peng et al. 2016, manuscript submitted to *J. Atmos. Oceanic Technol.*), which become more dispersed by mixing later in the day. For cloudy conditions, the midday τ was 0.47, 0.59, 0.49, and 0.48 in winter, spring, summer, and autumn, respectively. For rain or snow days, the monthly midday τ is much lower: 0.10–0.47.

The increasing emission of anthropogenic aerosols caused by the ever-growing population and human activities in Shanghai has resulted in the frequent occurrence of haze, especially during autumn and winter (Qian et al. 2015). Haze aerosols reflect, scatter, and absorb the solar radiation resulting in a decrease of $K_\downarrow$ reaching the surface. When clear days are stratified by the presence (or absence) of haze, its effects on solar radiation can be assessed (Fig. 5). For the study period, τ is decreased by about 0.07 (11.3% of the hourly average 0.65) between those hours with and without haze.

In terms of seasonal patterns, under clear-sky conditions the median τ increases steadily with solar elevation angle from 4° to 60° (Fig. 5e); with solar elevation angles $> 60°$, τ becomes constant (with values around 0.67). Under cloudy-sky conditions, the variation of τ with solar elevation is similar, but with values of τ decreased by 0.12. For rainy conditions, there is no obvious variation of τ with solar elevation, with values varying from 0.1 to 0.19. When clear-sky days are stratified into those with and without haze (Table 1), when the solar elevation angle is below 60°, τ is further attenuated by haze by 0.07 (~11.6%). However, when the solar elevation angle is larger than 60°, the impact of haze is less, with τ under haze conditions even slightly larger than when there is no haze. This may be a consequence of multiple scattering enhancing diffuse radiation receipt.

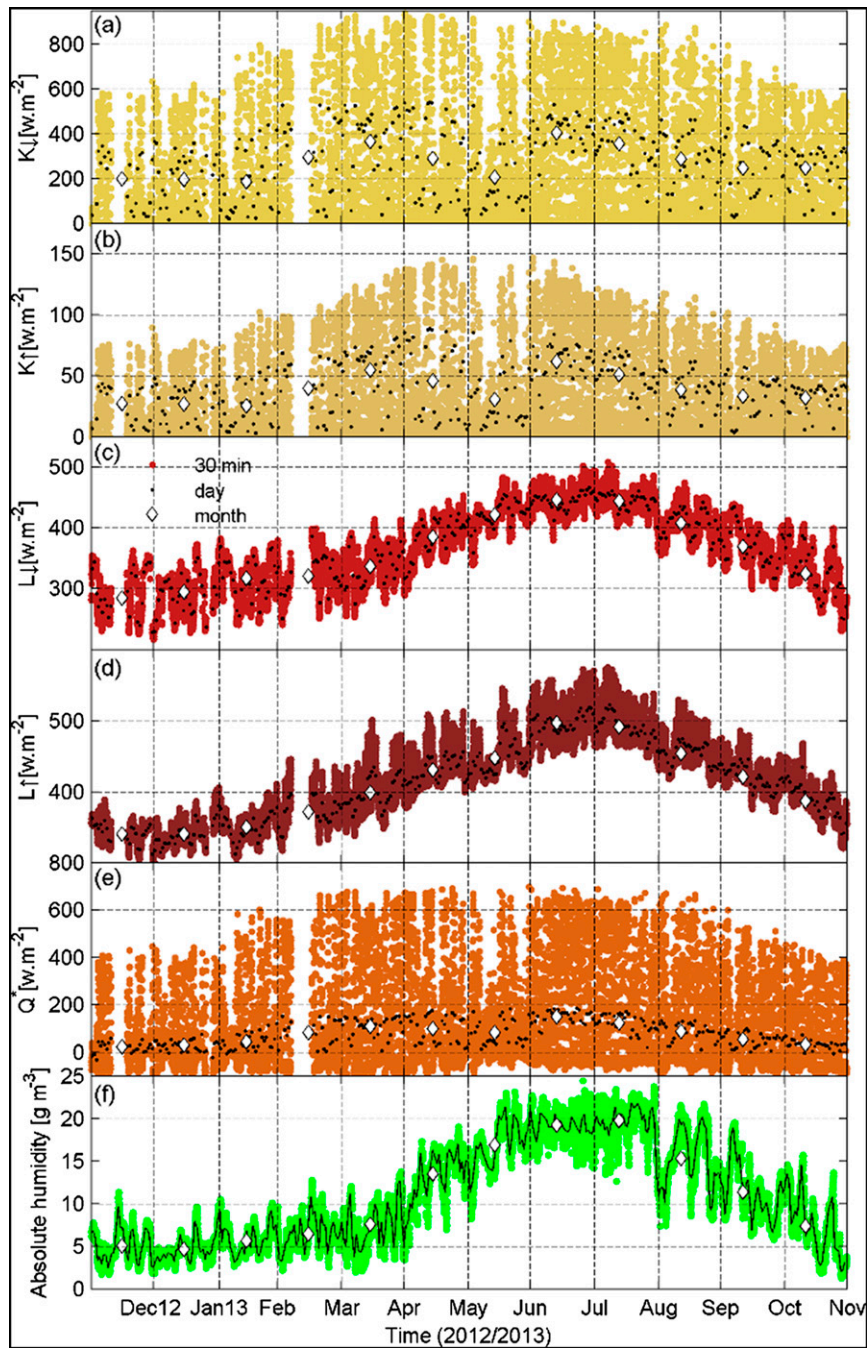The monthly median $PM_{2.5}$ concentrations (Fig. 4b) were higher from November to April than from May to

FIG. 1. Observed 30-min fluxes (colored dots) from the tower for (a) incoming shortwave radiation ($K_\downarrow$), (b) outgoing shortwave radiation ($K_\uparrow$), (c) incoming longwave radiation ($L_\downarrow$), (d) outgoing longwave radiation ($L_\uparrow$), and (e) net all-wave radiation (Q^*) in Shanghai (2012/13) with monthly (white diamonds) and daily (black dots; shortwave radiation for sunlight hours) means. Also shown is (f) hourly (green dots) and daily-mean (solid line) absolute humidity calculated using observed data at the automated weather station at XJH at 2 m above ground. The white diamonds in (f) are again monthly means.
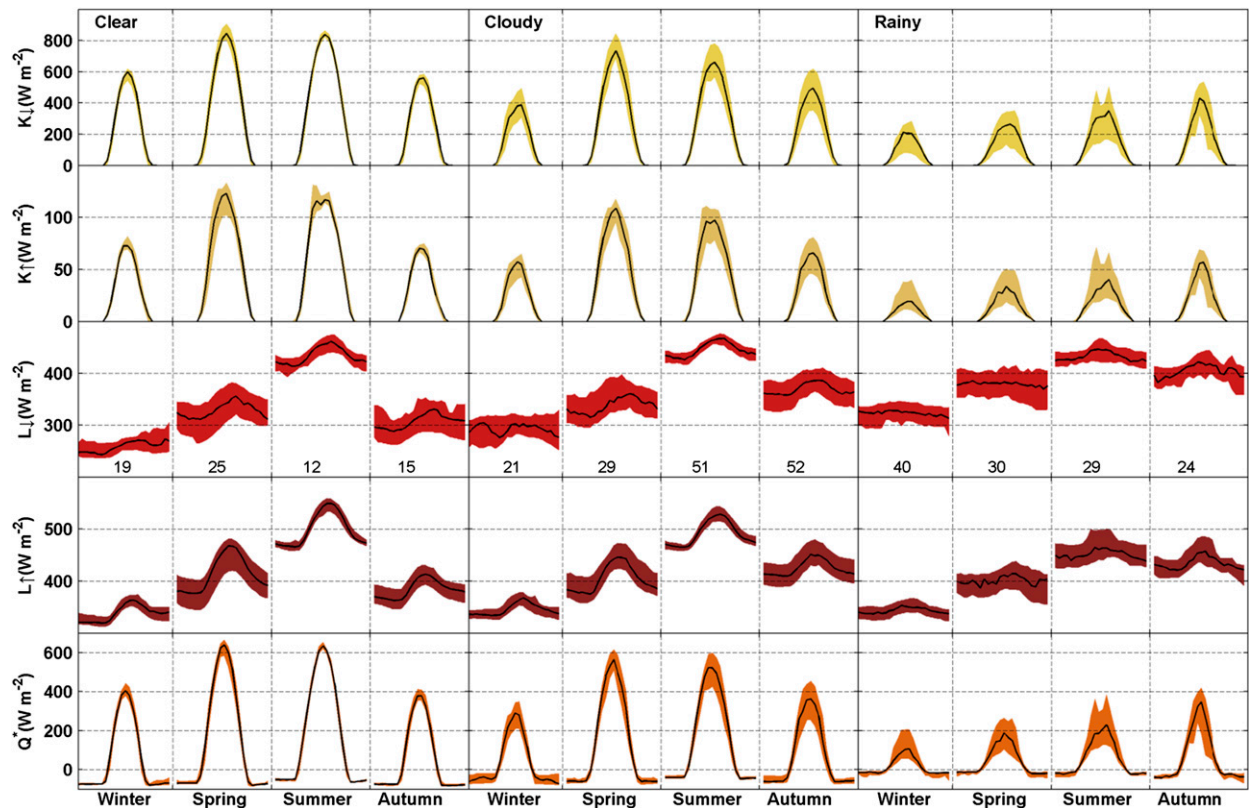
FIG. 2. Seasonal median diurnal (solid lines) radiation fluxes under (left) clear, (center) cloudy, and (right) rainy conditions with IQR (shaded). The number of days per season per sky condition is given in the middle row.

October. This is attributed to boundary layer dynamics and the effects of different large-scale synoptic systems affecting the Shanghai area in these two periods (Zhang et al. 2010). During the period of higher concentrations (November–April), the synoptic situation is generally less variable with northwesterly or northerly winds, which import $PM_{2.5}$ into Shanghai. In contrast, during the less polluted period, the main synoptic control is the

TABLE 1. Data availability for different cloud-cover (CC) conditions by month. Days are classified as clear or cloudy using manually observed cloud observations at 0800 and 1400 LST taken at the site. Clear days are subdivided into haze or no-haze hours on the basis of hourly visibility and humidity data.

| Class (units)	Definition	Frequency											
		Dec	Jan	Feb	Mar	Apr	May	Jun	Jul	Aug	Sep	Oct	Nov
Data availability													
Radiation data available (%)	Max: 48 day^{-1} × n days per month	57	82	90	61	95	89	85	96	97	93	91	97
Frequency of cloud conditions and definition (days)													
Clear days (71 days)	Daytime CC < 20%/ diurnal curve of $K_\downarrow$ very smooth	7	8	4	9	10	6	2	4	6	1	2	12
Cloudy (140 days)	Daytime CC 30%–80%	6	8	4	6	13	9	10	24	16	15	17	12
Overcast (13 days)	Daytime CC > 80%	0	3	0	0	0	1	0	0	1	4	2	2
Rainy (123 days)	Rain during 24 h	11	9	20	9	7	14	18	3	8	10	10	4
Clear hours daytime (total: 1549 h)													
Clear no-haze (313 h)	Hourly: visibility >10 km and $PM_{2.5}$ < 35 μg m^{-3}	0	0	13	41	30	44	0	53	70	12	22	28
Clear haze (796 h)	Hourly: visibility <10 km, RH < 90%, and $PM_{2.5}$ > 35 μg m^{-3}	96	100	65	86	120	99	46	3	19	6	22	134
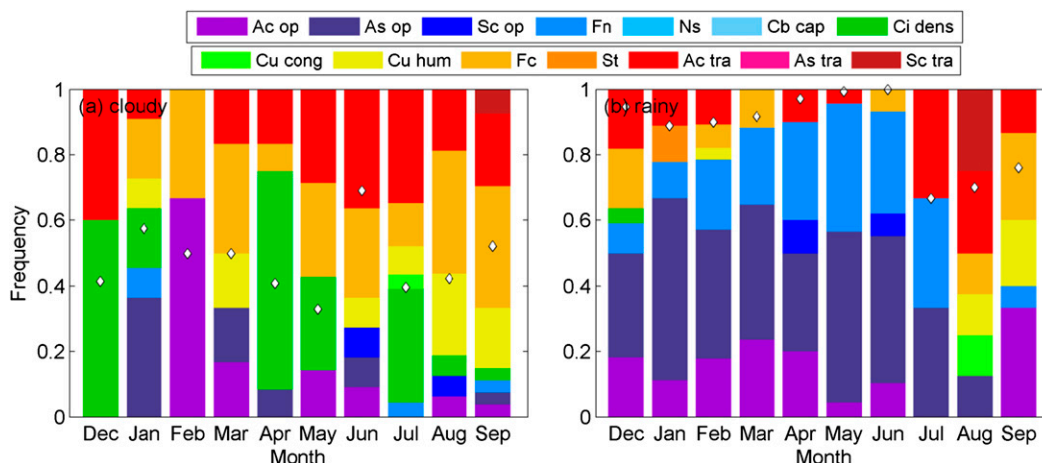
FIG. 3. Frequency of 14 cloud types [see World Meteorological Organization (1975) for cloud classification and code definitions] at 0800 LST at XJH by month for the study period (December 2012–September 2013) under (a) cloudy and (b) rainy conditions. The mean cloud fraction by month (white diamonds) is also shown. In October 2013, manual cloud observations ceased at this site.

subtropical high pressure belt, with low pressure troughs and typhoon systems. These synoptic systems tend to be associated with relatively strong easterly or southeasterly winds, which can transport ''clean air'' into coastal Shanghai from the sea and dilute the pollution generated in the city. The diurnal variation of τ for haze and no-haze conditions (Table 1) for these two periods is shown in Figs. 5a–e. Under clear-sky conditions in winter, τ was consistently smaller (by about 0.09) for haze conditions (Fig. 5a). This represents a 12.9% decrease in τ and daytime shortwave radiation receipt. However, the difference is less (11.2%) during the summer (Fig. 5b). This is attributed to greater visibility

(Figs. 5f,g) and much lower concentrations of $PM_{2.5}$ (Figs. 5j,k). Moreover, the stronger convection of the atmosphere in summer results in greater dilution of near-surface $PM_{2.5}$. Thus the measured near-surface $PM_{2.5}$ probably is not as representative of the total column $PM_{2.5}$ in summer than in winter when stagnant weather and inversion layers occur more frequently (Zhang and Cao 2015). Under cloudy-sky conditions, τ was even larger under haze conditions in winter (Fig. 5c) and consistently smaller in summer (Fig. 5d). As cloudy conditions have a wider range of cloud-cover fraction (0.2–0.8), the haze influence may be affected by the cloud-cover effect. The controls on atmospheric
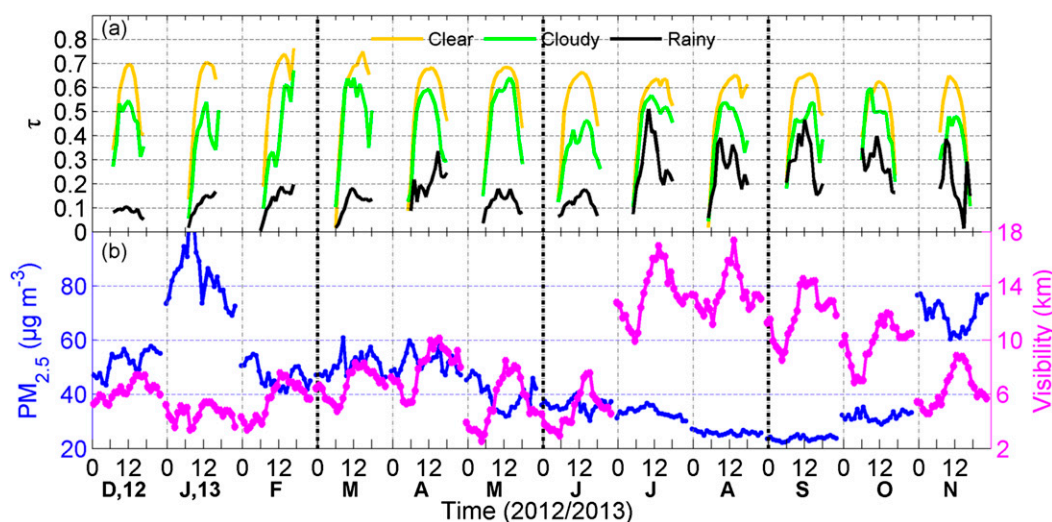

FIG. 4. Median monthly diurnal transmissivity (τ) on (a) clear (haze and no haze combined), cloudy, and precipitation days. (b) The $PM_{2.5}$ concentration (observed 50 m from XJH) and visibility (observed at 2 m at XJH by a Vaisala PWD22).
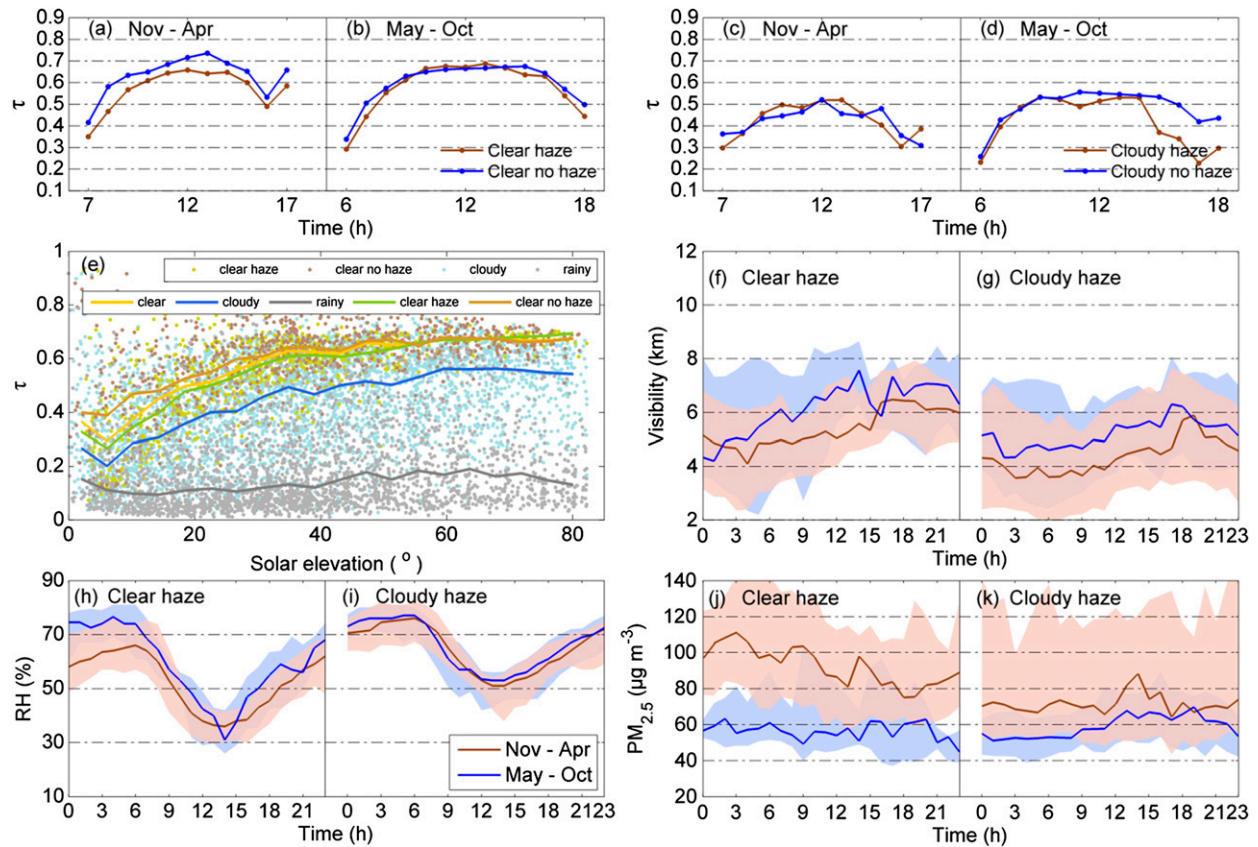
FIG. 5. Median diurnal transmissivity (τ) under clear haze and clear no-haze conditions: (a) November–April and (b) May–October. (c),(d) As in (a) and (b) but for cloudy haze and cloudy no-haze conditions. (e) The 30-min (dots) and median [lines, with 4°-bin midpoints plotted (i.e., the value at 2° represents 0°–4°)] τ as a function of solar elevation angle under clear skies (median only), clear haze, clear no-haze, cloudy, and rainy conditions. (f),(g) Median (lines) and IQR (shading) diurnal visibility (observed at 2 m at XJH by a Vaisala PWD22) by time of year (November–April, brown; May–October, blue) during clear and cloudy haze conditions (visibility < 10 km), respectively. (h),(i) As in (f) and (g), but for RH. (j),(k) As in (f) and (g), but for $PM_{2.5}$.

chemistry and haze are more complex than just synoptic conditions and wind directions. Changes in temperature, moisture, radiation, stability, boundary layer depth, and emissions (quantity and types) all will impact atmospheric chemistry with feedbacks to the radiative fluxes and hence τ. A more comprehensive explanation of the radiation forcing of haze conditions needs further detailed analysis of the chemical compositions of $PM_{2.5}$ and the meteorological conditions.

b. Characterization of the longwave radiation

Variations in incoming longwave radiation ($L_\downarrow$) are primarily correlated with near-surface air temperature, sky-view factor, water vapor, and the existence of mid- or low-level clouds (Flerchinger et al. 2009; Wang and Dickinson 2013). Thus, the annual variation of the observed $L_\downarrow$ in Shanghai is very similar to that of the air temperature. The lowest monthly mean $L_\downarrow$ was observed in December 2012 and January 2013 (284 and 294 W m^{-2}), the two coldest months in the observation period. The

highest monthly mean $L_\downarrow$ was observed in July and August (446 and 444 W m^{-2}, respectively). At this site, the daily maxima of $L_\downarrow$ varied from 382 W m^{-2} in winter to 509 W m^{-2} in summer (Fig. 1). Diurnal patterns under clear-sky conditions also are mostly governed by diurnal temperature variations.

In general, cloud cover enhances $L_\downarrow$ (Fig. 6), while the increase is smaller in spring (median diurnal: 2–19 W m^{-2}) and summer (5–18 W m^{-2}) than in winter (6–56 W m^{-2}) and autumn (49–71 W m^{-2}). This variability is a response to the water content (Fig. 1f) and cloud cover of the atmosphere. The average increases under cloudy relative to clear conditions for the four seasons (winter, spring, summer, and autumn) are about 30, 18, 15, and 60 W m^{-2}, with increases greater again for rainy conditions, except for summer (53, 50, 5, and 88 W m^{-2} for the four seasons, respectively). This effect of rainy days is undoubtedly due to the more extensive cloud cover. The reductions of $L_\downarrow$ under rainy conditions by about 1–21 W m^{-2} (diurnal median) from 1000 to 2100 LST in summer may be caused
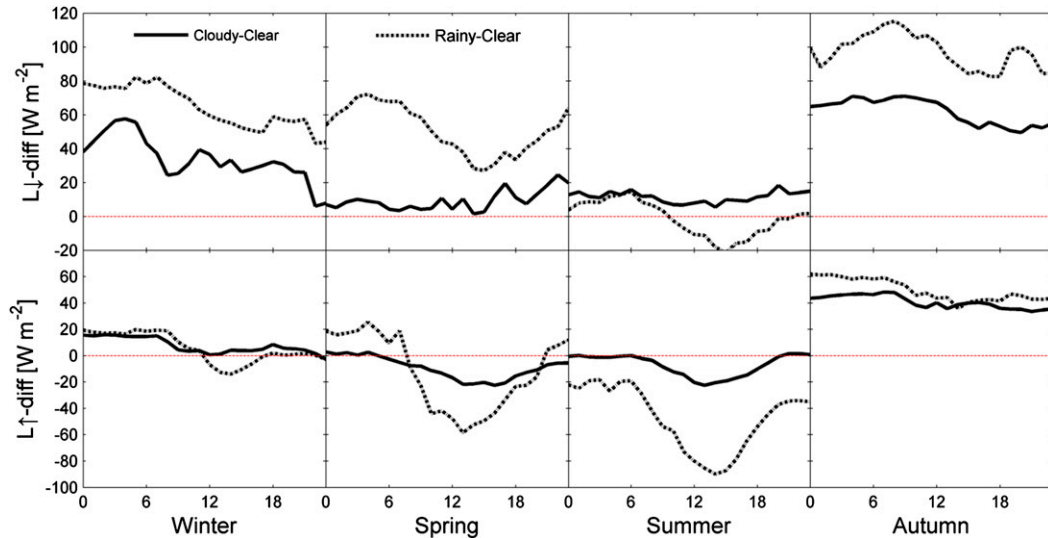
FIG. 6. Seasonal differences between the diurnal medians of cloudy and clear conditions and rainy and clear conditions for (top) $L_\downarrow$ and (bottom) $L_\uparrow$.

by lower air temperatures on these days than under clear conditions. For example, June was cool with 18 rainy days and only 2 clear days, as compared with the warmer and drier July and August (3 and 8 rainy days; 4 and 6 clear days, respectively).

Outgoing longwave radiation ($L_\uparrow$) is directly influenced by the urban surface temperature. Thus it depends on the amount of the total incoming radiation energy, $Q_\downarrow = K_\downarrow + L_\downarrow$, the conduction and convection heat exchange processes at the surface, and the nature of the urban surface facets. The annual pattern of $L_\uparrow$ is even more similar to the annual pattern of near-surface air temperature than $L_\downarrow$ (Fig. 1; cf. Fig. 3 in Ao et al. 2016).

As net all-wave radiation Q^* (Figs. 1 and 2) combines the four radiative components, it responds to the sun's elevation, surface characteristics, and cloud cover. Median daily maximum values in Shanghai under clear conditions range from $400\,\mathrm{W\,m^{-2}}$ in winter to $640\,\mathrm{W\,m^{-2}}$ in spring. The monthly average Q^* remains positive throughout the year. However, during winter months, radiative cooling exceeds the gain from solar input for

individual days. Hence daily average Q^* can become negative. The median diurnal pattern of Q^* under different sky conditions was, as expected, similar to $K_\downarrow$.

c. Surface albedo

Surface albedo α, a key parameter in numerical prediction models, influences radiative exchanges between the surface and the atmosphere (Liu et al. 2008). Figure 7 shows the median diurnal variations of surface albedo by season under different sky conditions when both $K_\downarrow$ and $K_\uparrow$ were $>2\,\mathrm{W\,m^{-2}}$. Overall, the albedo has the typical diurnal U shape pattern observed at other urban sites (e.g., Aida 1982). When the sun elevation is low ($<8°$) near sunrise and sunset, the surface albedo is >0.2, while the values are lower and almost constant during the middle of the day. In the morning the albedo is usually larger than in the afternoon, with an obvious increase around 0800 or 0900 LST from May to August. This is evident under both clear and cloudy conditions in summer (Fig. 7). This may be due to the effect of shadows in the afternoon (further discussed below) as documented elsewhere for other urban areas with deep
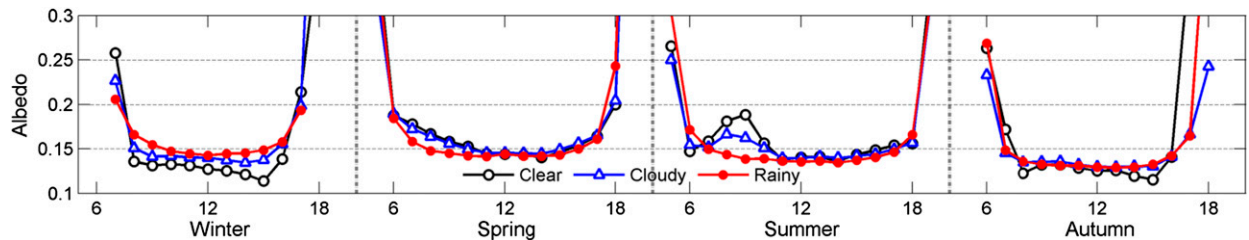

FIG. 7. Median diurnal variations of surface albedo (α) under clear, cloudy, and rainy conditions (Table 1). See Fig. 2 for the number of each type of day in each season.
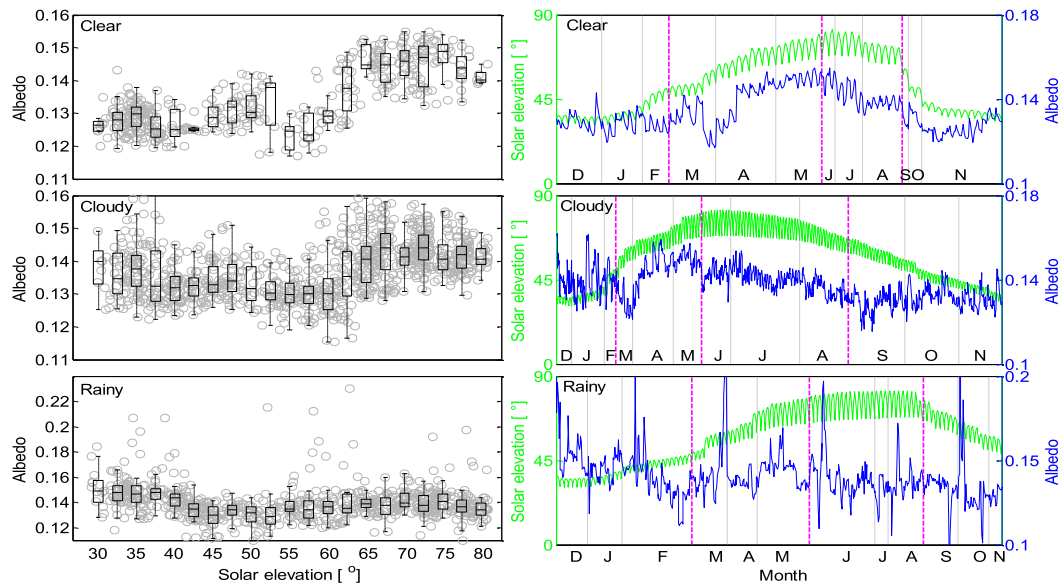
FIG. 8. (left) Variation of 30-min surface albedo α near midday (1100–1300 LST) with solar elevation angle h stratified by sky conditions (Table 1). Box plots at 2.5° solar elevation intervals show median, IQR, and $1.5 \times$ IQR whiskers. (right) Time series of solar elevation angle and albedo, with gray vertical lines to indicate the end of each month (with pink lines to indicate the seasons); the varying frequency of conditions causes the time (x) axis to be inconsistent among rows.

canyons (Minnis et al. 1997; Grimmond et al. 2004; Zhang et al. 2013; Kotthaus and Grimmond 2014b).

The surface albedos under clear conditions near noon (1100–1300 LST) are 0.128, 0.141, 0.143, and 0.129 for winter, spring, summer, and autumn, respectively. The surface albedo under clear or cloudy conditions increases with solar elevation (Fig. 8), while under rainy conditions the albedo remains more constant through the year (0.146, 0.142, 0.137, and 0.132 for winter, spring, summer, and autumn, respectively). The relation between surface albedo and solar elevation under different sky conditions provides corroboration for remote sensing results (e.g., Lucht et al. 2000; Schaepman-Strub et al. 2006). Under rainy conditions the surface itself will be wet, so there is an expected decrease in surface albedo. However, again it should be noted that the sensor (notably the incoming shortwave sensor) may be impacted by water droplets for some of the time. Albedo increases with cloud fraction (at 1400 LST; the time in the middle of the day with direct cloud observations; Fig. 9), notably, when cloud fraction is >40%; below that the effect of solar elevation angle dominates (Fig. 9).The combined influence of solar geometry and sky conditions on the surface albedo is assessed by comparing the median α with solar elevation angle stratified by sky conditions (clear, cloudy, and rainy) and solar azimuth angle [easterly (E) and westerly (W); Fig. 9c]. Higher surface reflectances at lower solar

elevation angles can be caused by increased specular reflectance by urban materials such as glass and metal (Kotthaus and Grimmond 2014b). This, however, is not particularly evident here. The surface albedo has a sharp decrease when solar elevation angle rises from 0 to about 8° under all sky conditions. The surface α for solar elevation angles < 44° decreases from rainy to cloudy to clear conditions, whereas for solar elevation angles > 44° the inverse occurs, albeit the differences between conditions are smaller. Under clear conditions, α is strongly influenced by direct radiation reflection (assuming no shadows), while under rainy–cloudy conditions, diffuse radiation dominates (Lucht et al. 2000). The surface α varies with solar azimuth angle (simplified here to east and west) in correspondence with surface heterogeneity, under both clear and overcast conditions. This indicates that the urban canyon absorbs both direct and diffuse radiation. The surface appears less reflective (darker) when solar rays come from the west, as the shadows of many tall buildings (e.g., the Sports Hotel) are within a radius of 20–30 m of the tower in this direction. This results in trapping of shortwave radiation. Under rainy conditions, the difference in α is smaller between east and west and becomes constant with solar elevation angles > 40°. The dominance of diffuse radiation almost removes dependence on solar geometry.

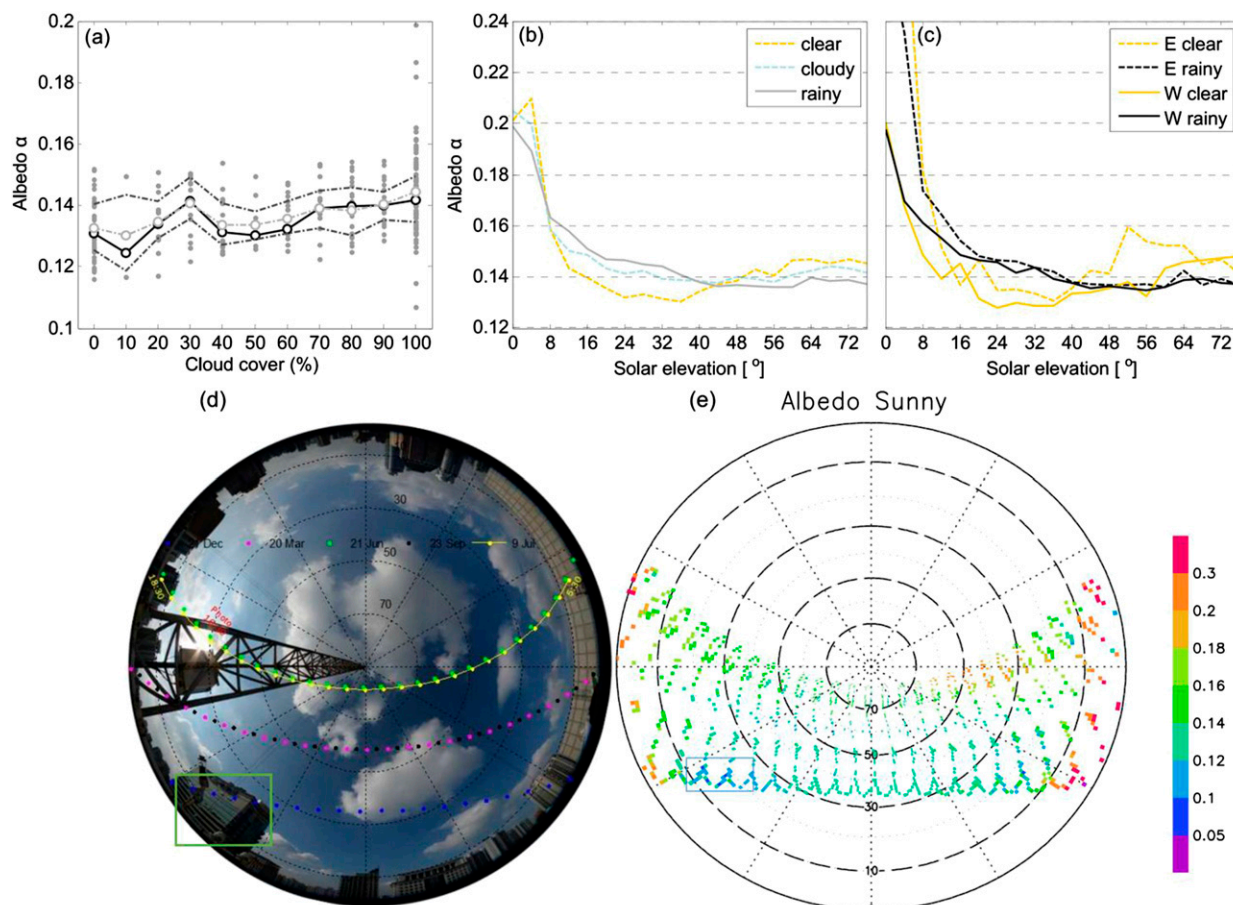Thus the larger range of α with solar elevation under clear conditions is attributed to building shadows

FIG. 9. Variation of surface albedo α (a) with cloud cover (manually observed at XJH) at 1400 LST from December 2012 to September 2013: daily (gray points), median (solid black line), mean (gray dash–dotted line), and IQR (the two black dash–dotted lines). Note that only three values occur in the 10% bin. Median albedo as a function of solar elevation angle (b) under clear, cloudy, and rainy conditions (Table 1) and (c) under sunny and rainy conditions stratified into sun in the east (E) and sun in the west (W), with 4°-bin points plotted (i.e., the value at 0° represents 0°–4°). (d) Fish-eye photograph taken at 1630 LST 9 Jul 2014 at the foot of the measurement tower: the position of the sun is indicated for every 30 min on the summer solstice (green dots), winter solstice (blue dots), vernal equinox (pink dots), and autumnal equinox (black dots) and on the day of the photograph (yellow line with dots), and the green rectangle contains the Sports Hotel. (e) Mean surface albedo [bins 1° solar elevation (radial) × 1° solar azimuth (angular) angle] as a function of sun position; the blue rectangle in lower left corresponds to the impact of the Sports Hotel.

increasing the spatial variability of surface conditions in the source area of the measurements. Analysis of fish-eye photographs taken at the foot of the tower show a significant surface element is the Sports Hotel located to the southwest (Fig. 9d; indicated by the green rectangle). The mean albedo (binned 1° elevation × 1° azimuth in Fig. 9e as a function of sun position) demonstrates the significantly lower albedo (Fig. 9e; indicated by the blue rectangle) in the late afternoon in winter seems to be caused by shadows from the Sports Hotel.

Despite significant variation of α with sky conditions and sun-surface geometry, a bulk surface albedo can be calculated to represent the overall characteristics of this site. The median all-sky value (solar elevation $> 20°$) α is 0.14 (IQR = 0.02). This is similar to values for other

central business districts [e.g., in London as reported in Kotthaus and Grimmond (2014a,b)].

Considering both transmissivity and albedo, the median τ increases from 0.15 to 0.45 with solar azimuth angle (65°–100°) in the morning (Fig. 10) and is asymmetric around noon. However, the afternoon slope decrease is flatter than in the morning. When stratified by seasons, the obvious increase of τ with azimuth angle between 235° and 255° seems to be related to the greater sky view in this direction, as no high buildings are present (fish-eye photograph in Fig. 9d). The median surface α is more variable when the sun is in the east than in the west. Overall, the surface albedo is larger near sunrise than near sunset. The seasonal variation of surface albedo as a function of solar azimuth angle is small.
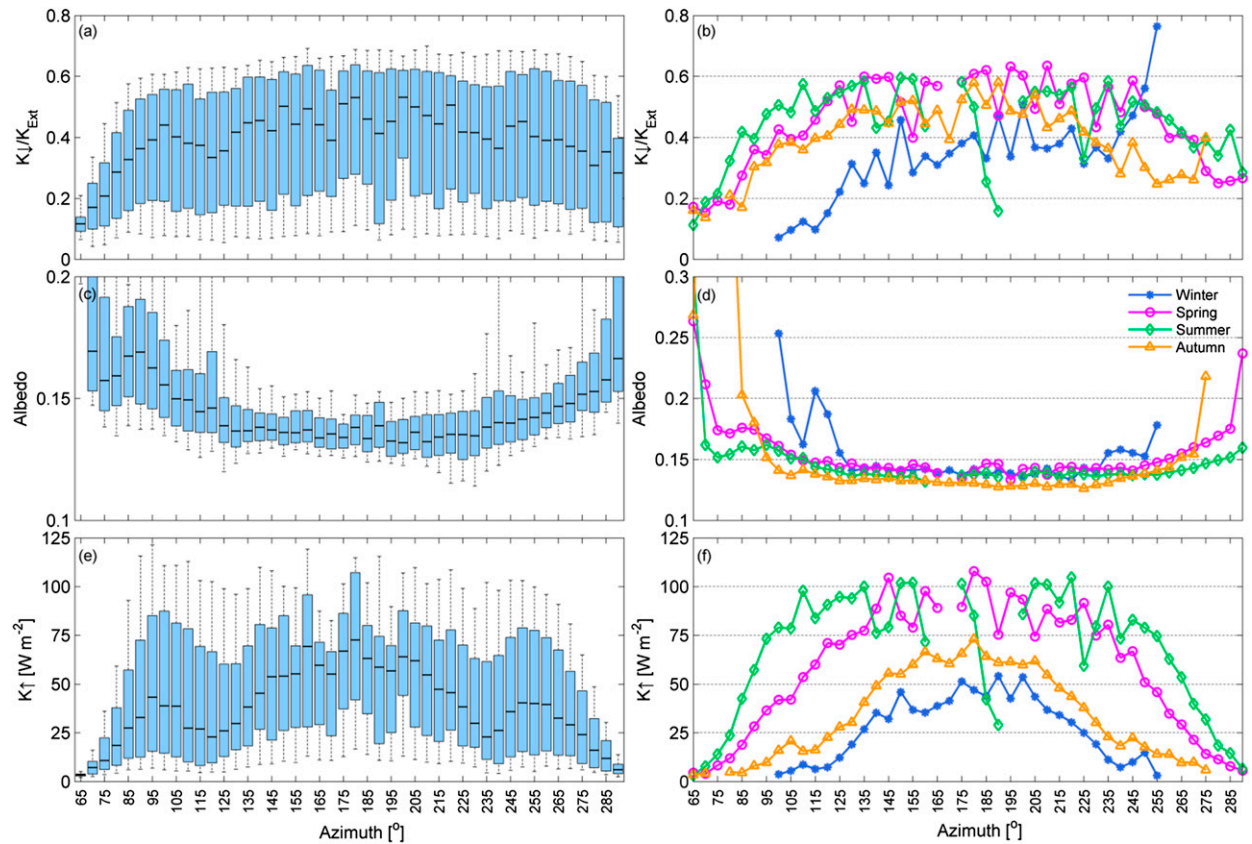
FIG. 10. Median (top) transmissivity, (middle) albedo, and (bottom) outgoing shortwave radiation as a function of solar azimuth angle (a),(c),(e) for the year, with the blue boxes indicating the IQR and the 10th and 90th percentiles given by the whiskers, and (b),(d),(f) by season.

d. Evaluation of a radiation parameterization scheme

Often direct measurements of radiative fluxes are unavailable so urban land surface schemes are used. Here the Shanghai data are used to evaluate the Net All-Wave Radiation Parameterization Scheme (NARP; Offerle et al. 2003; Loridan et al. 2011) within SUEWS (Järvi et al. 2011; Ward et al. 2016, version 2016a) using hourly data. The evaluation metrics used are the coefficient of determination (R^2), linear regression slope and intercept, root-mean-square error (RMSE), mean bias error (MBE), and mean absolute error (MAE):

$$\mathrm{RMSE} = \sqrt{\frac{1}{N} \sum_{i=1}^{N} (M_i - O_i)^2},$$

$$\mathrm{MBE} = \frac{1}{N} \sum_{i=1}^{N} (M_i - O_i), \quad \text{and}$$

$$\mathrm{MAE} = \frac{1}{N} |M_i - O_i|, \qquad (6)$$

where M_i are modeled values, O_i are observed values, and N is the number of data points. The metrics are calculated using hourly data ($N = 7365$) when no rainfall (hourly rainfall $= 0\,\mathrm{mm}$) was recorded.

The NARP local-scale (10^2–$10^4\,\mathrm{m}$) net all-wave radiation (Q^*) simulations require commonly measured meteorological variables and surface cover information. The outgoing shortwave radiation (Offerle et al. 2003) is determined using forcing provided by the downward shortwave radiation flux ($K_\downarrow$):

$$K_\uparrow = (f_i \alpha_i) K_\downarrow, \qquad (7)$$

where α_i is the surface albedo for each surface type i, which has fractional plan area f_i. The incoming long-wave radiation ($L_\downarrow$) is modeled using (Offerle et al. 2003)

$$L_\downarrow = \varepsilon_{\mathrm{sky}} \sigma T_{\mathrm{sky}}^4, \qquad (8)$$

where σ is the Stefan–Boltzmann constant ($\mathrm{W\,m^{-2}\,K^{-4}}$), T_{sky} is the bulk atmospheric temperature estimated as the measured air temperature T_a near the surface, and the atmospheric emissivity $\varepsilon_{\mathrm{sky}}$ is corrected from Prata's (1996) clear-sky $\varepsilon_{\mathrm{clear}}$ to account for cloud effects:

TABLE 2. SUEWS model input parameters by surface type (*i*): minimum ($\alpha_{i,\min}$) and maximum ($\alpha_{i,\max}$) albedo, emissivity (ε_i), and fraction of the *i*th surface (f_i). The surface fractions are for a circle of 500-m radius (about 80% eddy covariance flux source area) and of 80-m radius (100% radiation sensor FOV).

	Paved	Building	Evergreen trees/shrubs	Deciduous trees/shrubs	Grass	Bare soil	Water
$\alpha_{i,\min}$	0.12	0.18	0.1	0.12	0.18	0.21[a]	0.1[a]
$\alpha_{i,\max}$	0.14	0.18	0.1[b]	0.18[a]	0.21[a]	0.21[a]	0.1[a]
ε_i[a]	0.95	0.91	0.98	0.98	0.93	0.93	0.95
$f_{i\text{–}500\,\text{m}}$[c]	0.62	0.23	0.03	0.01	0.1	0	0.01
$f_{i\text{–}80\,\text{m}}$	0.51	0.38	0.02	0.01	0.08	0	0

[a] Data source: Oke (1987).
[b] Data source: Järvi et al. (2014).
[c] Data source: Ao et al. (2016).

$$\varepsilon_{\text{clear}} = 1 - (1 + w)\exp[-(1.2 + 3.0w)^{0.5}],$$
$$w = 46.5e_a/T_a, \quad \text{and}$$
$$\varepsilon_{\text{sky}} = \varepsilon_{\text{clear}} + (1 - \varepsilon_{\text{clear}})F_{\text{CLD}}, \tag{9}$$

where w is the precipitable water content (g cm^{-2}) approximated by atmospheric vapor pressure e_a and T_a, and F_{CLD} represents the cloud-cover fraction. In NARP, F_{CLD} can be estimated from measured $K_\downarrow$ or estimated as a function of RH and T_a (Loridan et al. 2011). The latter was used here:

$$F_{\text{CLD}}(\text{RH}, T_a) = 0.185[e^{(0.015 + 1.9\times10^{-4}T_a)\times\text{RH}} - 1]. \tag{10}$$

The above yields this parameterization for $L_\downarrow$,

$$L_\downarrow(e_a, T_a, \text{RH}) = \{\varepsilon_{\text{clear}}(e_a, T_a) + [1 - \varepsilon_{\text{clear}}(e_a, T_a)]$$
$$\times F_{\text{CLD}}(\text{RH}, T_a)\} \times \sigma T_a^4. \tag{11}$$

The surface outgoing longwave radiation ($L_\uparrow$) is estimated as (Offerle et al. 2003)

$$L_\uparrow = \varepsilon_0\sigma T_a^4 + 0.08K_\downarrow\left[1 - \left(\sum_{i=1}^{n} f_i\alpha_i\right)\right]$$
$$+ \left[1 - \left(\sum_{i=1}^{n} f_i\varepsilon_i\right)\right]L_\downarrow, \tag{12}$$

where ε_i are the surface emissivities for the component surface types and n is the number of surface types.

The 100% FOV (Schmid et al. 1991) for the radiometer used for the measurements has a radius of 80 m. The plan area surface characteristics were determined for this area and for 500 m around the site using the methods described in Ao et al. (2016). The latter area contributes to the eddy covariance (EC) flux measurements. These fractions were used with the other parameters (Table 2) for the model runs (1 December 2012–30 November 2013).

NARP/SUEWS successfully reproduces the diurnal cycle of fluxes (Fig. 11) with similar results for the two sets of plan area fractions [radiometer FOV (80 m) and EC source area (500 m)]. The seasonal mean daily maxima of $K_\uparrow$ are underestimated in spring and summer (i.e., negative MBE) and overestimated in winter and autumn (i.e., positive MBE) but there are high R^2 values (0.98–0.99) and small RMSE values [from 2.6 (winter) to 5.8 W m^{-2} (summer)]. Typically, the greatest deviation from 1:1 relations occurs in the early morning and late afternoon hours.

The diurnal cycle of downward longwave radiation ($L_\downarrow$) in spring and summer is reproduced relatively well by the model. The larger observed and simulated values occur in the afternoon. However, the amplitude of the diurnal variation was underestimated for all seasons. This is mainly because the range of modeled F_{CLD} based on Eq. (10) is too narrow (Ward et al. 2016). The RMSE for $L_\downarrow$ varies from 19.3 W m^{-2} (summer) to 29.3 W m^{-2} (winter). There is a positive bias for all seasons except winter. This change in positive to negative bias in winter was also documented in Baltimore, Maryland, and Lodz, Poland (Loridan et al. 2011). This may be due to the formulation of Eq. (10) for F_{CLD} being for a relatively narrow annual range of T_a observed in London, or a consequence of the form of the function (Ward et al. 2016). Lower (higher) bias may occur in colder (warmer) temperatures (Loridan et al. 2011).

Although the mean diurnal variation of outgoing longwave radiation $L_\uparrow$ is well simulated for all seasons, the mean daily maximum is overestimated in each season. The R^2 varies from 0.84 to 0.97, RMSE varies from 7.8 to 10 W m^{-2}, MBE varies from 1.7 to 4.1 W m^{-2}, and MAE varies from 5.6 to 7.1 W m^{-2}.

The net result is that SUEWS/NARP underestimates the mean daytime in all seasons and overestimates nighttime Q^*. The overall RMSE for Q^* is 26–27.8 W m^{-2}, and the MAE is 21–24.5 W m^{-2} for all seasons. The MBE for Q^* is negative in winter (-10.7 W m^{-2}), and positive in spring (1.8 W m^{-2}), summer (8.9 W m^{-2}), and autumn (3.2 W m^{-2}). The overall performance of NARP at the XJH site is comparable to
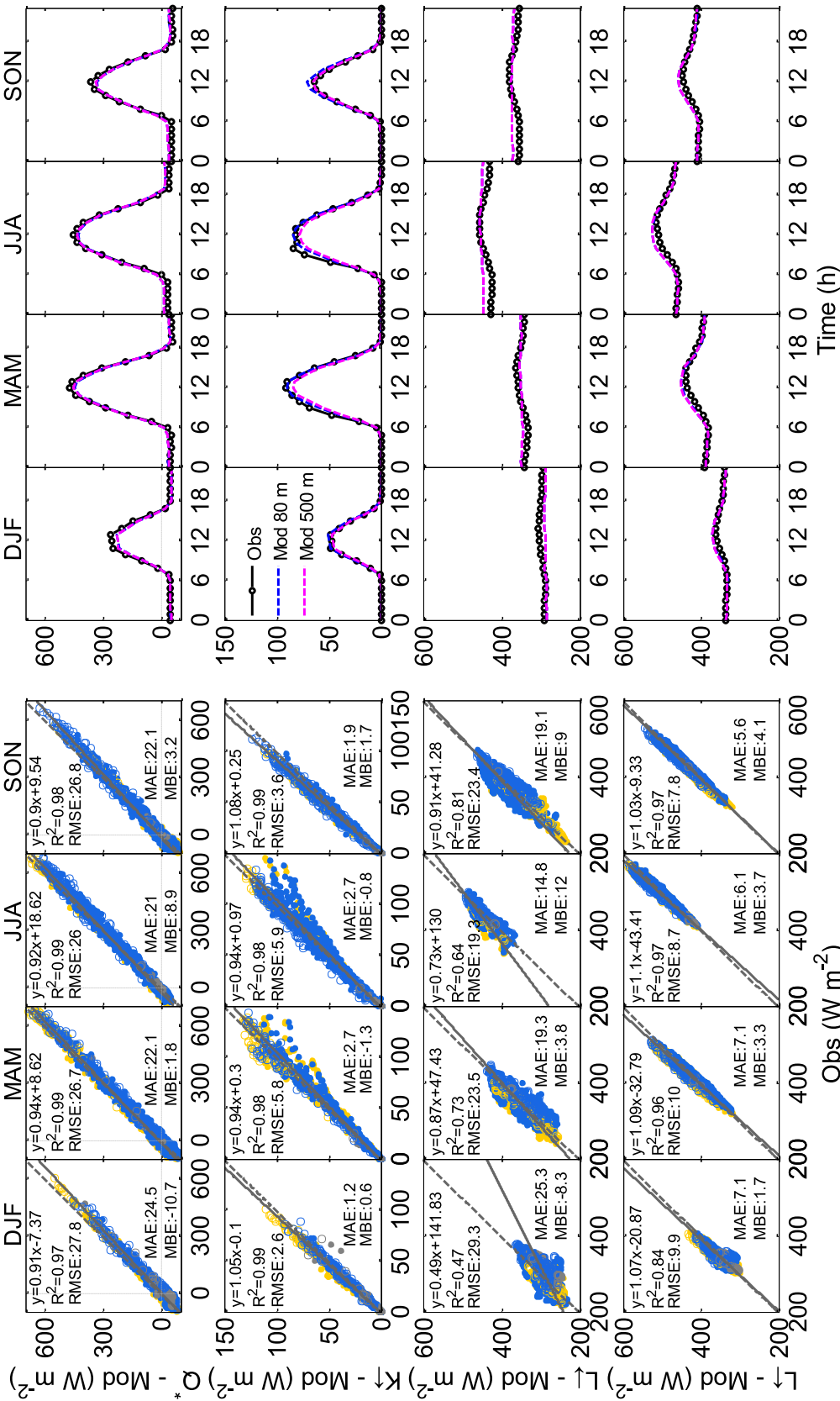
FIG. 11. Observed and modeled radiation fluxes at the XJH site by season: shown at left are results for an FOV of 80 m for the midday hours 1100–1300 LST (open circles) and other hours (filled circles) under clear-sky (yellow), cloudy (blue), and rainy (gray) conditions, with performance metrics under all-sky conditions also given [the linear regression (equation and solid lines; dashed line indicates 1:1), the coefficient of determination, and the MBE, MAE, and RMSE (the latter three in watts per meter squared)], and shown at the right is mean diurnal behavior modeled using parameters for an FOV of 80 m (blue) and an FOV of 500 m (pink), along with the observations (black).

that at other more northerly and non-Asian city sites (e.g., Loridan et al. 2011).

4. Conclusions

From analysis of radiative fluxes stratified by sky conditions for a central business district of Shanghai the key findings are as follows:

- Given the latitude of this site, the annual range of median daytime maxima of incoming solar radiation [from 575 (winter) to 875 W m^{-2} (spring)] is much smaller than for higher-latitude cities, as expected.
- Cloud-cover fraction and type both have a significant impact on the radiation fluxes. In Shanghai, this is especially evident in June with the East Asian rainy season when opacus clouds are frequent. Most evident is the reduction of incoming shortwave radiation in June by 350 W m^{-2}. As expected, the radiative fluxes are more variable, as quantified by the IQR, under cloudy and rainy conditions than for clear conditions.
- Incoming longwave radiation is larger under cloudy conditions, as expected, thereby reducing radiative cooling at night. The average increase relative to clear-sky conditions for the four seasons (winter, spring, summer, autumn) was about 30, 18, 15, and 60 W m^{-2} and 53, 50, 5, and 88 W m^{-2} under cloudy and rainy conditions, respectively.
- Median daily maximum values of $Q*$ under clear conditions range from about 400 (winter) to 640 W m^{-2} (spring).
- Midday (1100–1300 LST) incoming shortwave radiation normalized by the total solar radiation flux received at the top of Earth's atmosphere ranged between 0.6 and 0.7 under clear conditions, and decreased steadily from winter to spring to summer to autumn (0.69, 0.68, 0.64, and 0.63). Under cloudy conditions, the midday τ values were 0.47, 0.59, 0.49, and 0.48 in winter, spring, summer, and autumn, respectively. For rainy days, the monthly midday τ values were often much lower, from 0.10 to 0.47.
- Increased atmospheric aerosol loading under haze conditions results in a decrease of τ by about 0.07 (11.3%).
- Midday surface albedo values under clear conditions are 0.128, 0.141, 0.143, and 0.129 for winter, spring, summer, and autumn, respectively. There is a strong positive correlation with the solar elevation angle. The surface α for solar elevation angles $< 44°$ decreases from rainy to cloudy to clear conditions, whereas for solar elevation angles $> 44°$ the inverse occurs, albeit the differences for the cloud conditions are smaller.

- As cloud-cover fraction increases, the surface albedo is impacted, especially when cloud fraction is larger than 40%. The lower albedo values calculated during summer were caused by higher transmissivity with larger incoming shortwave radiation flux.
- The surface albedo varies most with solar elevation angle and azimuth angle because of the heterogeneity of the urban surface at this site. A bulk surface albedo of 0.14 was calculated to represent the overall characteristics of this site across radiative conditions. This is similar to other dense cities.
- Individual tall buildings casting shadows have a dominant impact, reducing the albedo. This is particularly evident in the late afternoon (given the position of the buildings relative to the measurement site) and in winter (with lower solar elevation angles).
- The observed data, when used to evaluate the NARP submodel of SUEWS, show that NARP/SUEWS can reproduce the overall net all-wave radiation fluxes at this site well. However, more attention needs to be directed to the longwave fluxes in conditions of high humidity.

These radiation measurements are the first full year of data published for a central business district in China. The results are important in filling the gap of long-term radiation measurements in East Asian and low-latitude cities and provide a dataset for evaluation of a range of urban land surface schemes of broad utility to urban planners and decision-makers.

REFERENCES

Aida, M., 1982: Urban albedo as a function of the urban structure—A model experiment. *Bound.-Layer Meteor.*, **23**, 405–413, doi:10.1007/BF00116269.
——, and K. Gotoh, 1982: Urban albedo as a function of the urban structure—A two-dimensional numerical simulation. *Bound.-Layer Meteor.*, **23**, 415–424, doi:10.1007/BF00116270.

Akbari, H., S. Bretz, D. M. Kurn, and J. Hanford, 1997: Peak power and cooling energy savings of high-albedo roofs. *Energy Build.*, **25**, 117–126, doi:10.1016/S0378-7788(96)01001-8.

——, H. D. Matthews, and D. Seto, 2012: The long-term effect of increasing the albedo of urban areas. *Environ. Res. Lett.*, **7**, 024004, doi:10.1088/1748-9326/7/2/024004.

Ao, X., and Coauthors, 2016: Heat, water and carbon exchanges in the tall megacity of Shanghai: Challenges and results. *Int. J. Climatol.*, doi:10.1002/joc.4657, in press.

Blonquist, J. M., Jr., B. D. Tanner, and B. Bugbee, 2009: Evaluation of measurement accuracy and comparison of two new and three traditional net radiometers. *Agric. For. Meteor.*, **149**, 1709–1721, doi:10.1016/j.agrformet.2009.05.015.

Bretz, S. E., and H. Akbari, 1997: Long-term performance of high-albedo roof coatings. *Energy Build.*, **25**, 159–167, doi:10.1016/S0378-7788(96)01005-5.

Chen, L., E. Ng, X. An, C. Ren, M. Lee, U. Wang, and Z. He, 2012: Sky view factor analysis of street canyons and its implications for daytime intra-urban air temperature differentials in high-rise, high-density urban areas of Hong Kong: A GIS-based simulation approach. *Int. J. Climatol.*, **32**, 121–136, doi:10.1002/joc.2243.

Christen, A., and R. Vogt, 2004: Energy and radiation balance of a central European city. *Int. J. Climatol.*, **24**, 1395–1421, doi:10.1002/joc.1074.

Ding, A. J., and Coauthors, 2013: Intense atmospheric pollution modifies weather: A case of mixed biomass burning with fossil fuel combustion pollution in eastern China. *Atmos. Chem. Phys.*, **13**, 10 545–10 554, doi:10.5194/acp-13-10545-2013.

Eva, H., and E. F. Lambin, 1998: Burnt area mapping in central Africa using ATSR data. *Int. J. Remote Sens.*, **19**, 3473–3497, doi:10.1080/014311698213768.

Flerchinger, G. N., W. Xaio, D. Marks, T. J. Sauer, and Q. Yu, 2009: Comparison of algorithms for incoming atmospheric long-wave radiation. *Water Resour. Res.*, **45**, W03423, doi:10.1029/2008WR007394.

Fu, Q. Y., 2009: Emission inventory and formation mechanism of high pollution of fine particulate matters in Shanghai. Ph.D. dissertation, Fudan University, 158 pp.

Grimmond, C. S. B., C. Souch, and M. D. Hubble, 1996: Influence of tree cover on summertime surface energy balance fluxes, San Gabriel Valley, Los Angeles. *Climate Res.*, **6**, 45–57, doi:10.3354/cr006045.

——, S. K. Potter, H. N. Zutter, and C. Souch, 2001: Rapid methods to estimate sky-view factors applied to urban areas. *Int. J. Climatol.*, **21**, 903–913, doi:10.1002/joc.659.

——, J. A. Salmond, T. R. Oke, B. Offerle, and A. Lemonsu, 2004: Flux and turbulence measurements at a densely built-up site in Marseille: Heat, mass (water and carbon dioxide), and momentum. *J. Geophys. Res.*, **109**, D24101, doi:10.1029/2004JD004936.

He, Q., C. Li, F. Geng, H. Yang, P. Li, T. Li, D. Liu, and Z. Pei, 2012: Aerosol optical properties retrieved from Sun photometer measurements over Shanghai, China. *J. Geophys. Res.*, **117**, D16204, doi:10.1029/2011JD017220.

Jacobson, M. Z., 2005: *Fundamentals of Atmospheric Modeling.* 2nd ed. Cambridge University Press, 828 pp.

Järvi, L., C. S. B. Grimmond, and A. Christen, 2011: The Surface Urban Energy and Water Balance Scheme (SUEWS): Evaluation in Los Angeles and Vancouver. *J. Hydrol.*, **411**, 219–237, doi:10.1016/j.jhydrol.2011.10.001.

——, ——, M. Taka, A. Nordbo, H. Setälä, and I. B. Strachan, 2014: Development of the Surface Urban Energy and Water Balance

Scheme (SUEWS) for cold climate cities. *Geosci. Model Dev.*, **7**, 1691–1711, doi:10.5194/gmd-7-1691-2014.

Jiang, Y., X. Liu, X.-Q. Yang, and M. Wang, 2013: A numerical study of the effect of different aerosol types on East Asian summer clouds and precipitation. *Atmos. Environ.*, **70**, 51–63, doi:10.1016/j.atmosenv.2012.12.039.

Kipp & Zonen, 2014: CNR 4 net radiometer instruction manual. 37 pp. [Available online at http://www.kippzonen.com/Download/354/Manual-CNR-4-Net-Radiometer-English.]

Kondo, A., M. Ueno, A. Kaga, and K. Yamaguchi, 2001: The influence of urban canopy configuration on urban albedo. *Bound.-Layer Meteor.*, **100**, 225–242, doi:10.1023/A:1019243326464.

Kopp, G., and J. L. Lean, 2011: A new, lower value of total solar irradiance: Evidence and climate significance. *Geophys. Res. Lett.*, **38**, L01706, doi:10.1029/2010GL045777.

Kotthaus, S., and C. S. B. Grimmond, 2014a: Energy exchange in a dense urban environment—Part I: Temporal variability of long-term observations in central London. *Urban Climate*, **10**, 261–280, doi:10.1016/j.uclim.2013.10.002.

——, and ——, 2014b: Energy exchange in a dense urban environment—Part II: Impact of spatial heterogeneity of the surface. *Urban Climate*, **10**, 281–307, doi:10.1016/j.uclim.2013.10.001.

——, T. E. L. Smith, M. J. Wooster, and C. S. B. Grimmond, 2014: Derivation of an urban materials spectral library through emittance and reflectance spectroscopy. *ISPRS J. Photogramm. Remote Sens.*, **94**, 194–212, doi:10.1016/j.isprsjprs.2014.05.005.

Li, D., E. Bou-Zeid, and M. Oppenheimer, 2014: The effectiveness of cool and green roofs as urban heat island mitigation strategies. *Environ. Res. Lett.*, **9**, 055002, doi:10.1088/1748-9326/9/5/055002.

——, T. Sun, M. Liu, L. Yang, L. Wang, and Z. Gao, 2015: Contrasting responses of urban and rural surface energy budgets to heat waves explain synergies between urban heat islands and heat waves. *Environ. Res. Lett.*, **10**, 054009, doi:10.1088/1748-9326/10/5/054009.

Li, H., Q. Zhang, and S. Wang, 2010: Research on characteristics of land-surface radiation and heat budget over the Loess Plateau of central Gansu in summer (in Chinese). *Adv. Earth Sci.*, **25**, 1070–1081, doi:10.11867/j.issn.1001-8166.2010.10.1070.

Li, J.-J., X.-R. Wang, X.-J. Wang, W.-C. Ma, and H. Zhang, 2009: Remote sensing evaluation of urban heat island and its spatial pattern of the Shanghai metropolitan area, China. *Ecol. Complexity*, **6**, 413–420, doi:10.1016/j.ecocom.2009.02.002.

Liu, H., G. Tu, and W. Dong, 2008: Three-year changes of surface albedo of degraded grassland and cropland surfaces in a semiarid area. *Chin. Sci. Bull.*, **53**, 1246–1254, doi:10.1007/s11434-008-0171-2.

Loridan, T., and Coauthors, 2010: Trade-offs and responsiveness of the single-layer urban canopy parametrization in WRF: An offline evaluation using the MOSCEM optimization algorithm and field observations. *Quart. J. Roy. Meteor. Soc.*, **136**, 997–1019, doi:10.1002/qj.614.

——, C. S. B. Grimmond, B. D. Offerle, D. T. Young, T. E. L. Smith, L. Järvi, and F. Lindberg, 2011: Local-Scale Urban Meteorological Parameterization Scheme (LUMPS): Long-wave radiation parameterization and seasonality-related developments. *J. Appl. Meteor. Climatol.*, **50**, 185–202, doi:10.1175/2010JAMC2474.1.

Lucht, W., C. B. Schaaf, and A. H. Strahler, 2000: An algorithm for the retrieval of albedo from space using semiempirical BRDF models. *IEEE Trans. Geosci. Remote Sens.*, **38**, 977–998, doi:10.1109/36.841980.

Mackey, C. W., X. Lee, and R. B. Smith, 2012: Remotely sensing the cooling effects of city scale efforts to reduce urban heat island. *Build. Environ.*, **49**, 348–358, doi:10.1016/j.buildenv.2011.08.004.

Masson, V., 2000: A physically-based scheme for the urban energy budget in atmospheric models. *Bound.-Layer Meteor.*, **94**, 357–397, doi:10.1023/A:1002463829265.

Miao, S., J. Dou, F. Chen, J. Li, and A. Li, 2012: Analysis of observations on the urban surface energy balance in Beijing. *Sci. China Earth Sci.*, **55**, 1881–1890, doi:10.1007/s11430-012-4411-6.

Michel, D., R. Philipona, C. Ruckstuhl, R. Vogt, and L. Vuilleumier, 2008: Performance and uncertainty of CNR1 net radiometers during a one-year field comparison. *J. Atmos. Oceanic Technol.*, **25**, 442–451, doi:10.1175/2007JTECHA973.1.

Minnis, P., S. Mayor, W. L. Smith, and D. F. Young, 1997: Asymmetry in the diurnal variation of surface albedo. *IEEE Trans. Geosci. Remote Sens.*, **35**, 879–890, doi:10.1109/36.602530.

Moriwaki, R., and M. Kanda, 2004: Seasonal and diurnal fluxes of radiation, heat, water vapor, and carbon dioxide over a sub-urban area. *J. Appl. Meteor.*, **43**, 1700–1710, doi:10.1175/JAM2153.1.

Nie, W., and Coauthors, 2014: Polluted dust promotes new particle formation and growth. *Sci. Rep.*, **4**, 6634, doi:10.1038/srep06634.

Offerle, B., C. S. B. Grimmond, and T. R. Oke, 2003: Parameterization of net all-wave radiation for urban areas. *J. Appl. Meteor.*, **42**, 1157–1173, doi:10.1175/1520-0450(2003)042<1157:PONARF>2.0.CO;2.

Oke, T. R., 1982: The energetic basis of the urban heat island. *Quart. J. Roy. Meteor. Soc.*, **108**, 1–24, doi:10.1002/qj.49710845502.

——, 1987: *Boundary Layer Climates*. 2nd ed. Routledge, 435 pp.

Prata, A. J., 1996: A new long-wave formula for estimating downward clear-sky radiation at the surface. *Quart. J. Roy. Meteor. Soc.*, **122**, 1127–1151, doi:10.1002/qj.49712253306.

Qian, J., H. Zhu, W. He, J. Huang, J. Xu, and G. Li, 2015: Shanghai fog and haze weather characteristics and influencing factors (in Chinese). *Shanghai Energy Conserv.*, **45**, 424–430. [Available online at http://en.cnki.com.cn/Article_en/CJFDTotal-SHJL201508009.htm.]

Qian, Y., D. P. Kaiser, L. R. Leung, and M. Xu, 2006: More frequent cloud-free sky and less surface solar radiation in China from 1955 to 2000. *Geophys. Res. Lett.*, **33**, L01812, doi:10.1029/2005GL024586.

Raman, A. P., M. A. Anoma, L. Zhu, E. Rephaeli, and S. Fan, 2014: Passive radiative cooling below ambient air temperature under direct sunlight. *Nature*, **515**, 540–544, doi:10.1038/nature13883.

Roberts, S. M., 2010: Three-dimensional radiation flux source areas in urban areas. Ph.D. dissertation, University of British Columbia, 214 pp.

Schaepman-Strub, G., M. E. Schaepman, T. H. Painter, S. Dangel, and J. V. Martonchik, 2006: Reflectance quantities in optical remote sensing—Definitions and case studies. *Remote Sens. Environ.*, **103**, 27–42, doi:10.1016/j.rse.2006.03.002.

Schmid, H. P., H. A. Cleugh, C. S. B. Grimmond, and T. R. Oke, 1991: Spatial variability of energy fluxes in suburban terrain. *Bound.-Layer Meteor.*, **54**, 249–276, doi:10.1007/BF00183956.

Shi, J., and L. Cui, 2012: Characteristics of high impact weather and meteorological disaster in Shanghai, China. *Nat. Hazards*, **60**, 951–969, doi:10.1007/s11069-011-9877-6.

Sigma, 2013: Large aperture F3.5 circular fisheye lens with close up capability, optimized for use with digital SLR cameras. [Available online at http://www.sigma-photo.co.jp/english/lens/wide/8_35/.]

Soux, A., J. A. Voogt, and T. R. Oke, 2004: A model to calculate what a remote sensor 'sees' of an urban surface. *Bound.-Layer Meteor.*, **112**, 401–424, doi:10.1023/B:BOUN.0000027978.21230.b7.

Steyn, D. G., J. E. Hay, I. D. Watson, and G. T. Johnson, 1986: The determination of sky-view factors in urban environments using video imagery. *J. Atmos. Oceanic Technol.*, **3**, 759–764, doi:10.1175/1520-0426(1986)003<0759:TDOSVF>2.0.CO;2.

Sun, T., C. S. B. Grimmond, and G.-H. Ni, 2016: How do green roofs mitigate urban thermal stress under heat waves? *J. Geophys. Res.*, **121**, 5320–5335, doi:10.1002/2016JD024873.

Tan, J., and Coauthors, 2015: Urban integrated meteorological observations: Practice and experience in Shanghai, China. *Bull. Amer. Meteor. Soc.*, **96**, 85–102, doi:10.1175/BAMS-D-13-00216.1.

Wang, H., Z. Hu, W. Ma, and D. Li, 2008: The seasonal variation of microclimate characteristics and energy transfer in the surface layer over Dingxin Gobi (in Chinese). *Chin. J. Atmos. Sci.*, **32**, 1458–1470. [Available online at http://en.cnki.com.cn/Article_en/CJFDTOTAL-DQXK200806020.htm.]

Wang, K., and R. E. Dickinson, 2013: Global atmospheric downward longwave radiation at the surface from ground-based observations, satellite retrievals, and reanalyses. *Rev. Geophys.*, **51**, 150–185, doi:10.1002/rog.20009.

——, P. Wang, J. Liu, M. Sparrow, S. Haginoya, and X. Zhou, 2005: Variation of surface albedo and soil thermal parameters with soil moisture content at a semi-desert site on the western Tibetan Plateau. *Bound.-Layer Meteor.*, **116**, 117–129, doi:10.1007/s10546-004-7403-z.

——, J. Augustine, and R. E. Dickinson, 2012a: Critical assessment of surface incident solar radiation observations collected by SURFRAD, USCRN and AmeriFlux networks from 1995 to 2011. *J. Geophys. Res.*, **117**, D23105, doi:10.1029/2012JD017945.

——, R. E. Dickinson, M. Wild, and S. Liang, 2012b: Atmospheric impacts on climatic variability of surface incident solar radiation. *Atmos. Chem. Phys.*, **12**, 9581–9592, doi:10.5194/acp-12-9581-2012.

Wang, X., X. Sun, J. Tang, and X. Yang, 2015: Urbanization-induced regional warming in Yangtze River delta: Potential role of anthropogenic heat release. *Int. J. Climatol.*, **35**, 4417–4430, doi:10.1002/joc.4296.

Ward, H. C., J. G. Evans, and C. S. B. Grimmond, 2013: Multi-season eddy covariance observations of energy, water and carbon fluxes over a suburban area in Swindon, UK. *Atmos. Chem. Phys.*, **13**, 4645–4666, doi:10.5194/acp-13-4645-2013.

——, S. Kotthaus, L. Järvi, and C. S. B. Grimmond, 2016: Surface Urban Energy and Water Balance Scheme (SUEWS): Development and evaluation at two UK sites. *Urban Climate*, doi:10.1016/j.uclim.2016.05.001, in press.

Wild, M., 2012: Enlightening global dimming and brightening. *Bull. Amer. Meteor. Soc.*, **93**, 27–37, doi:10.1175/BAMS-D-11-00074.1.

World Meteorological Organization, 1975: International cloud atlas: Manual on the observation of clouds and other meteors. WMO Rep. 407, 155 pp.

Xiao, Z.-M., Y.-F. Zhang, S.-M. Hong, X.-H. Bi, L. Jiao, Y.-C. Feng, and Y.-Q. Wang, 2011: Estimation of the main factors influencing haze, based on a long-term monitoring campaign in Hangzhou, China. *Aerosol Air Qual. Res.*, **11**, 873–882, doi:10.4209/aaqr.2011.04.0052.

Zhang, G.-L., X.-R. Zhen, J.-G. Tan, and J. Yin, 2010: The analysis of the relationship between the air quality in Shanghai and surface pressure patterns and meteorological factors (in Chinese). *J. Trop. Meteor.*, **26**, 124–128. [Available online at http://en.cnki.com.cn/Article_en/CJFDTOTAL-RDQX201001019.htm.]

Zhang, Y.-F., X.-P. Wang, Y.-X. Pan, and R. Hu, 2013: Diurnal and seasonal variations of surface albedo in a spring wheat field of arid lands of northwestern China. *Int. J. Biometeor.*, **57**, 67–73, doi:10.1007/s00484-012-0534-x.

Zhang, Y.-L., and F. Cao, 2015: Fine particulate matter ($PM_{2.5}$) in China at a city level. *Sci. Rep.*, **5**, 14884, doi:10.1038/srep14884.

Zhao, W., N. Zhang, J. Sun, and J. Zou, 2014: Evaluation and parameter-sensitivity study of a single-layer urban canopy model (SLUCM) with measurements in Nanjing, China. *J. Hydrometeor.*, **15**, 1078–1090, doi:10.1175/JHM-D-13-0129.1.

Zhou, D., S. Zhao, L. Zhang, G. Sun, and Y. Liu, 2015: The footprint of urban heat island effect in China. *Sci. Rep.*, **5**, 11160, doi:10.1038/srep11160.